AIAA 99–1394
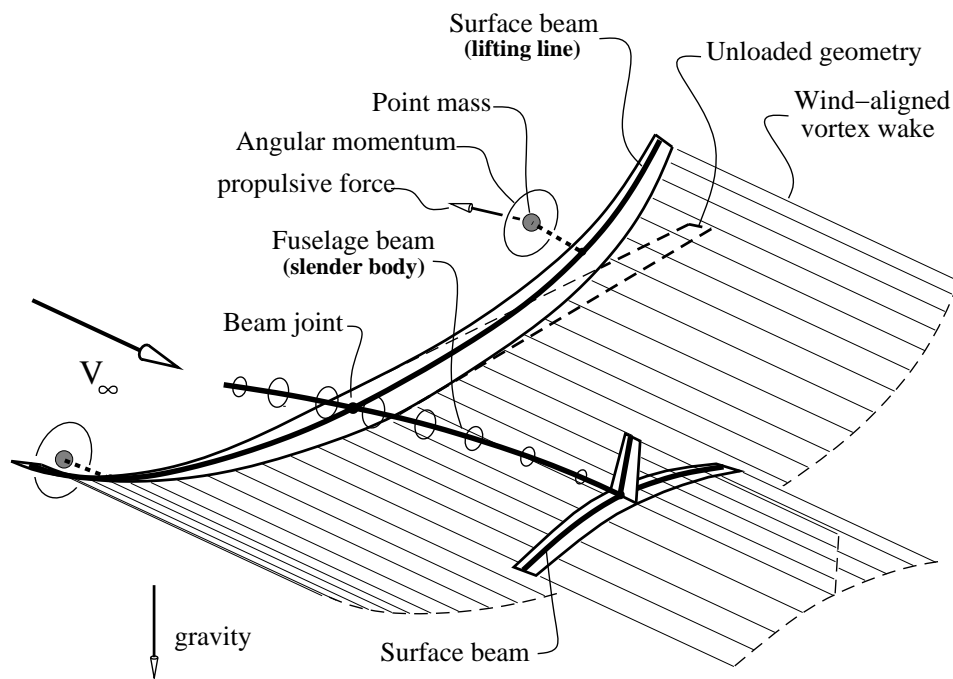
Integrated Simulation Model for Preliminary Aerodynamic, Structural, and Control-Law Design of Aircraft

Mark Drela

MIT Department of Aeronautics and Astronautics
Cambridge, MA 02139

40th AIAA SDM Conference
April 12–15, 1999/St.Louis, MO

INTEGRATED SIMULATION MODEL FOR PRELIMINARY AERODYNAMIC, STRUCTURAL, AND CONTROL-LAW DESIGN OF AIRCRAFT

Mark Drela [*]

MIT Department of Aeronautics and Astronautics
Cambridge, MA 02139

Abstract

An integrated model is developed for aerodynamic, structural, and control simulation of flexible aircraft in extreme flight situations. The structure consists of joined nonlinear beams allowing arbitrarily large deformations. The aerodynamic model is a compressible vortex/source-lattice with wind-aligned trailing vorticity. Full unsteady terms with flight dynamics are included. Model forcing is via gusts or control inputs.

The overall nonlinear equation set is solved by a full Newton method. The Newton Jacobian matrix is also used for frequency-domain computations to investigate flight stability, control-response behavior, and flutter. Nonlinear performance of control laws can be examined.

The numerical problem is small enough for interactive computation, allowing rapid diagnosis of local aerodynamic stall, structural failure, or control system saturation for a wide range of flight conditions. The overall approach allows quick generation of a robust multi-disciplinary preliminary design which can serve as a good basis for subsequent detailed design.

Nomenclature

Coordinates and dimensions

X, Y, Z	inertial (absolute) earth coordinates
x, y, z	aircraft body coordinates
c, s, n	local coordinates fixed to beam section
c_{cg}, n_{cg}	c, n locations of mass centroid
c_{ta}, n_{ta}	c, n locations of tension axis
$\bar{c}$	local wing chord
$\bar{x}_o$	location of s axis from leading edge
R	local slender-body radius
ℓ	streamwise distance
t	time
$\bar{\bar{T}}$	axis transformation tensor
i	node index along beam; $\sqrt{-1}$
θ	spanwise Glauert coordinate

Structural variables and parameters

$\vec{r}, \vec{u}, \vec{\omega}$	beam-section location, velocity, rotation
$\vec{v}, \vec{a}$	beam-section absolute velocity, acceleration
φ, ϑ, ψ	beam-section orientation Euler angles in $\vec{\theta}$
$\vec{F}, \vec{M}$	beam-stress force, moment resultants
ϵ_s	beam-axis extensional strain
$\kappa_c, \kappa_s, \kappa_n$	beam-axis c, s, n curvatures
EA	beam extensional stiffness
$EI_{cc} \ldots$	beam bending stiffness matrix components
$\bar{\bar{K}}$	curvature/angle-rate relation tensor
μ	section mass/length density
$\bar{\bar{\iota}}$	section c, s, n inertia/length tensor
$\vec{g}$	gravitational acceleration

Aerodynamic variables and parameters

α_A	2-D airfoil lift-curve intercept
$dc_\ell/d\alpha$	2-D airfoil lift-curve slope
c_{d_f}, c_{d_p}	2-D section friction, pressure drag coeffs.
c_m	2-D section pitching moment coefficient
$dc_\ell/d\delta_F$	2-D section flap lift derivative
$dc_m/d\delta_F$	2-D section flap moment derivative
$\delta_{F1}, \delta_{F2} \ldots$	control deflections
A_k	circulation Fourier mode coefficients
$\vec{V}_{\text{ind}}$	local induced velocity
V_∞, α, β	freestream speed and flow angles
$\vec{w}_k, \vec{w}_\infty$	induced-velocity influence functions
ρ	air density
Γ	bound circulation
λ	Prandtl-Glauert factor $= 1/\sqrt{1 - M_\infty^2}$

Global variables and operating parameters

$\vec{R}, \vec{U}, \vec{\Omega}$	aircraft absolute position, velocity, rotation
Φ, Θ, Ψ	aircraft orientation Euler angles in $\vec{\Theta}$

Introduction

Aircraft design is inherently a multi-disciplinary task, where aerodynamic, structural, and control system designs must be integrated and any conflicts resolved. Although making the tradeoffs between aerodynamic performance and structural weight (e.g. optimum aspect ratio) is relatively straightforward in the static case, the possibility of flutter or unfavorable cou-

---

[*]Associate Professor, AIAA Associate Fellow

pling between structural modes and the control laws greatly complicates this problem.

Current aircraft dynamics analysis systems, such as NASTRAN,[1] are typically assembled from separate general-purpose structural and aerodynamic analyses, coupled through interpolated influence matrices. To get a managable problem size, flutter or forced-response analyses are performed via a modal approach, using the lowest structural modes as a solution basis. This technique is general and powerful, but its generality carries a price — significant effort is needed to generate and analyze a case. The reliance on influence matrices makes analysis of large-deflection nonlinear problems especially awkward. These difficulties significantly hamper preliminary design studies, where it is advantageous to consider as many candidate designs and operating conditions as possible.

The alternative approach presented here simplifies the overall aircraft system description to the greatest extent possible, while still capturing the relevant physics. Johnson[2] and Minguet[3] have done related work for helicopter rotors, which exhibit strong coupling between the aerodynamics and structural dynamics. The author's precursor work[4] considered the steady case for a single beam/wing. This proved to be effective for design of flexible lightweight wings for human-powered aircraft and high-altitude drones. The present work is a major extension, with multiple beams and a full unsteady treatment included. Because all components are modeled as beams and lifting lines, the approach is inherently limited to moderate or high aspect ratios. The overall physical model is shown visually in Figure 1, and its key features are summarized below.
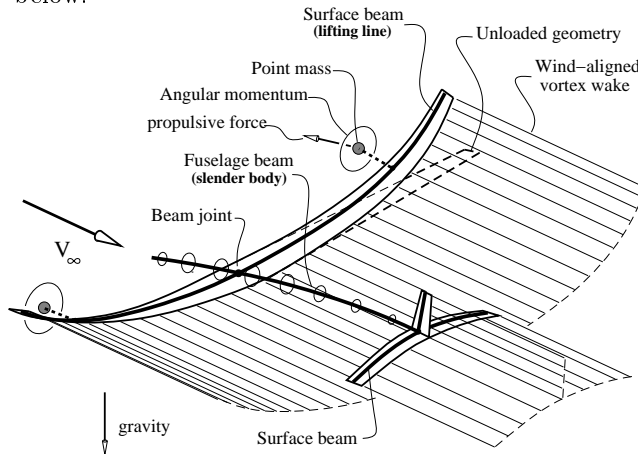

Fig. 1   Configuration representation

Structures. General nonlinear unsteady bending/torsion beams, connected by joints. Arbitrary mass, inertia, stiffness distributions. Points with mass, angular momentum, and propulsive forces.

Aerodynamics. Unsteady lifting lines with wind-aligned trailing vorticity. General section properties with control-surface deflection. Stall-model effects on lift and drag. Slender bodies with forces, moments, and volume displacement effects on flow. Prandtl-Glauert compressibility correction in wind axes.

Flight Dynamics. Overall body dynamics represented. Gust velocity field embedded in atmosphere.

Control. General state-feedback law drives control-surface deflections and thrust settings.

Rather than relying on coupling of these "disciplines" through influence matrices, the present approach simply treats *all* of the governing equations as a coupled nonlinear system, solved directly by a full Newton method. The one-dimensional description of the component beams gives a small state vector and fast solution, with no need for modal representations. The frequency-domain calculations make use of the system Jacobian matrix already available from the base nonlinear problem, giving further economy. Not using modal coordinates for flutter and forced-response predictions removes any uncertainties related to mode truncation or mode coupling.

The overall method is implemented in the program ASWING, which is aimed at effective preliminary aircraft design via rapid interactive setup, computation, and analysis. The remainder of the paper will summarize the physical models, numerical discretizations, and the solution techniques involved. Validation and application computations will be presented.

Axis Systems

The aircraft description uses three cartesian coordinate systems, XYZ, xyz, csn, shown in Figures 2, 3. The freestream velocity $\vec{V}_\infty$ is opposite the aircraft velocity $\vec{U}$, and is related to V_∞, α and β in the standard manner.

$$\vec{V}_\infty = V_\infty \begin{Bmatrix} \cos\alpha\,\cos\beta \\ -\sin\beta \\ \sin\alpha\,\cos\beta \end{Bmatrix} = -\vec{U} \qquad (1)$$

Local Beam Coordinates

The beam stress/strain and aerodynamic force relations are developed in the csn system, with s nearly parallel with the tension axis. The transformation of any vector from xyz to csn is via the rotation tensor $\bar{\bar{T}}$ formed from the local Euler angles φ, ψ, ϑ, applied in that order.

$$\bar{\bar{T}} = \begin{bmatrix} \cos\vartheta & 0 & -\sin\vartheta \\ 0 & 1 & 0 \\ \sin\vartheta & 0 & \cos\vartheta \end{bmatrix} \begin{bmatrix} \cos\psi & \sin\psi & 0 \\ -\sin\psi & \cos\psi & 0 \\ 0 & 0 & 1 \end{bmatrix} \begin{bmatrix} 1 & 0 & 0 \\ 0 & \cos\varphi & \sin\varphi \\ 0 & -\sin\varphi & \cos\varphi \end{bmatrix}$$
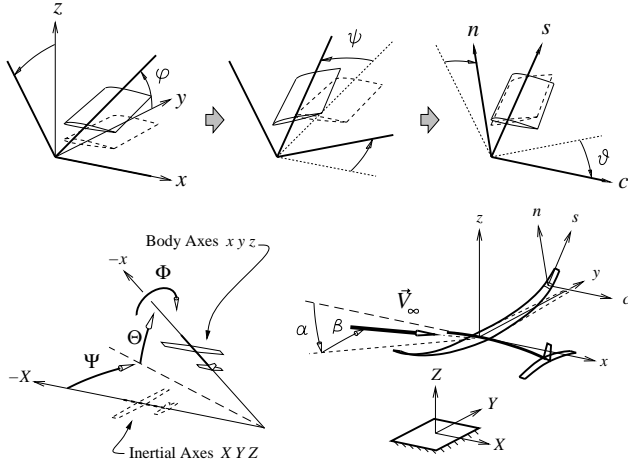
2

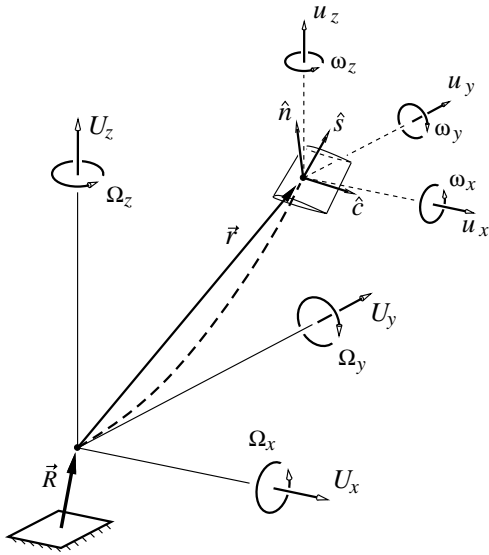**Fig. 2 Coordinate systems and Euler angles**

Fig. 3 Velocities and rotation rates.

Figure 2 shows the transformation sequence. The c, s, n beam curvatures are related to the rate of change of $\bar{\bar{T}}$ (κ_s is actually a twist rate).

$$-\vec{\kappa}_{csn} \times \bar{\bar{T}} = \frac{d\bar{\bar{T}}}{ds} \quad \rightarrow \quad \vec{\kappa}_{csn} = \bar{\bar{K}} \frac{d}{ds} \left\{ \begin{array}{c} \varphi \\ \vartheta \\ \psi \end{array} \right\}$$

$$\bar{\bar{K}} = \begin{bmatrix} \cos\psi\,\cos\vartheta & 0 & -\sin\vartheta \\ -\sin\psi & 1 & 0 \\ \cos\psi\,\sin\vartheta & 0 & \cos\vartheta \end{bmatrix}$$

The Euler angle sequence in Figure 2 has the usual polar singularity at $\psi = \pm 90°$. Using the alternative sequence ψ, φ, ϑ for fuselage beams avoids this problem.

Bending-Moment and Force Resultants

The bending moment and force resultants are considered in both xyz and csn axes, with $\bar{\bar{T}}$ relating the

two.

$$\vec{M}_{csn} = \bar{\bar{T}}\,\vec{M}_{xyz} \quad , \quad \vec{F}_{csn} = \bar{\bar{T}}\,\vec{F}_{xyz}$$

Figure 4 shows the sign conventions for the $\vec{M}$ and $\vec{F}$ components. Note that M_s is a torsion load while M_c and M_n are bending moments. Likewise, F_s is an axial load, while F_c and F_n are shear loads. Such interpretation cannot be made for the x, y, z components.
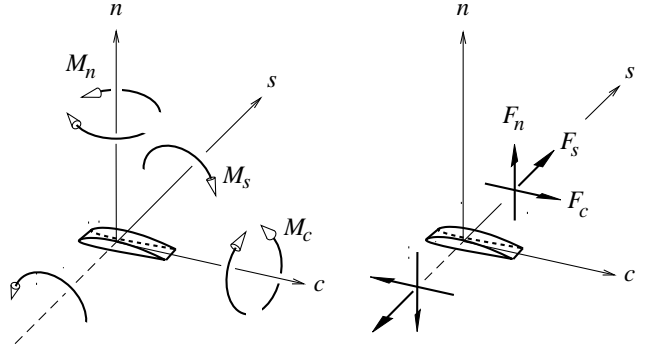

Fig. 4 Load resultants on element of beam.

Stress-Strain Beam Relations

A beam section is shown in Figure 5. The overall extensional strain at some location c, n is

$$\epsilon(c, n) = \epsilon_s + c\,(\kappa_n - \kappa_{n0}) - n\,(\kappa_c - \kappa_{c0})$$

where ϵ_s is the strain at the s axis, and κ_0 are the curvatures of the unloaded beam, calculated from the specified unloaded φ_0, ϑ_0, ψ_0 distributions (i.e. the jig shape). The axial force and moment vector are related to the beam extensional and curvatures via the bending-stiffness matrix $\bar{\bar{E}}$ (necessarily symmetric). Minguet[3] also considers the c, n shear strains. These will not be considered here.

$$F_s = EA\,\epsilon(c_{ta}, n_{ta}) \tag{2}$$
$$\vec{M}_{csn} = \bar{\bar{E}}\,\{\vec{\kappa} - \vec{\kappa}_0\}_{csn} \tag{3}$$

The tension axis location c_{ta}, n_{ta} is the usual modulus-weighted area centroid of the beam section. The six components of $\bar{\bar{E}}$, such as EI_{cc}, GJ, etc., are prescribed as one-dimensional functions along the beam.
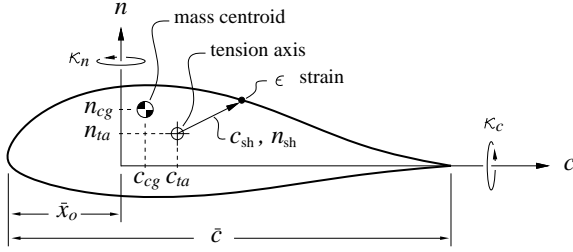
Force and Moment Equilibrium Relations

The force and moment balance on a beam element of length ds is expressed in the x, y, z axes as

$$d\vec{F} + \vec{f}\,ds + \Delta\vec{F}_P\,d(1) = 0 \tag{4}$$
$$d\vec{M} + \vec{m}\,ds + \Delta\vec{M}_P\,d(1) + d\vec{r} \times \vec{F} = 0 \tag{5}$$

where $\vec{f}$ and $\vec{m}$ are applied distributed loads, $\Delta\vec{F}_P$ and $\Delta\vec{M}_P$ are applied point loads, and $d(1)$ is the unit-impulse function.

Fig. 5 Beam section with curvatures and resulting strain.

Equations (3,4,5) are valid for arbitrarily large beam deformations, and for angle discontinuities such as dihedral breaks. For small deformations they become linear bending/torsion beam relations.

Discrete Formulation

The discrete representation of the beam is given by the 18 node variables

$$\vec{r}_i \qquad \vec{\theta}_i \qquad \vec{M}_i \qquad \vec{F}_i \qquad \vec{u}_i \qquad \vec{\omega}_i$$

where i is the node index along the beam. The Euler-angle triplet $\vec{\theta} = (\varphi, \vartheta, \psi)$ is not a proper vector, but serves as convenient shorthand. For steady or quasi-steady problems, $\vec{u}_i$ and $\vec{\omega}_i$ can be omitted, giving only 12 variables per node.

Box finite-difference discretization will be employed. For the present nonlinear problem it is extremely simple and 2nd-order accurate. It can also capture solution discontinuities with no special treatment. In the following development, every vector is assumed to be expressed in xyz axes unless subscripted by csn.

Interior Equations

The displacements and angles are related by three discrete compatibility relations

$$\Delta \vec{r} - \bar{\bar{T}}_a^T \left\{ 0 \quad 1+\epsilon_s \quad 0 \right\}_a^T \Delta s_0 = 0 \qquad (6)$$

where s_0 is the unloaded-beam arc length, and $\Delta(\ )$ is a difference and $(\ )_a$ is a simple average between the i and $i+1$ stations, e.g.

$$\Delta x = x_{i+1} - x_i \quad , \qquad \bar{\bar{T}}_a = \frac{1}{2}\left(\bar{\bar{T}}_{i+1} + \bar{\bar{T}}_i\right).$$

The axial strain in (6) is related to the local loads.

$$\epsilon_s = \left(\frac{F_s}{EA}\right)_a + \left(\left\{n_{ta} \quad 0 \quad -c_{ta}\right\} \bar{\bar{E}}^{-1} \vec{M}_{csn}^T\right)_a$$

Equations (3,4,5) are discretized as follows.

$$\bar{\bar{K}}_a \Delta\vec{\theta} - \bar{\bar{K}}_{a\,0} \Delta\vec{\theta}_0 - \bar{\bar{E}}_a^{-1} \bar{\bar{T}}_a \vec{M}_a \Delta s = 0 \quad (7)$$

$$\Delta\vec{M} + \vec{m}_a \Delta s + \Delta\vec{M}_P + \Delta\vec{r} \times \vec{F}_a = 0 \qquad (8)$$

$$\Delta\vec{F} + \vec{f}_a \Delta s + \Delta\vec{F}_P = 0 \qquad (9)$$

The loads $\vec{f}$, $\vec{m}$, $\Delta\vec{F}_P$, $\Delta\vec{M}_P$, will be derived shortly.

The discrete equilibrium equations (8,9) are strongly conservative, with no net force or moment being "lost" due to discretization errors. Discontinuities due to beam angle breaks or concentrated loads are captured perfectly simply by placing these on a zero-length interval with $\Delta s = 0$. The equations then automatically become the correct discontinuity-jump relations.

Kinematic Constraints

The equations governing $\vec{u}_i$ and $\vec{\omega}_i$, used only for unsteady cases, are direct kinematic constraints.

$$\frac{d}{dt}\vec{r}_i - \vec{u}_i = 0 \qquad (10)$$

$$\frac{d}{dt}\vec{\theta}_i - \left[\bar{\bar{T}}^T \bar{\bar{K}}\right]^{-1} \vec{\omega}_i = 0 \qquad (11)$$

Boundary Conditions and Constraints

Equations (6,7,8,9) require twelve appropriate boundary conditions to form a closed system. Typically these consist of six kinematic and six load conditions

$$\begin{array}{ll} \vec{r}_i = \vec{r}_{\mathrm{spec}} & , \qquad \vec{\theta}_i = \vec{\theta}_{\mathrm{spec}} \\ \vec{F}_i = \vec{F}_{\mathrm{spec}} & , \qquad \vec{M}_i = \vec{M}_{\mathrm{spec}} \end{array}$$

imposed at appropriate locations. These typically appear at the beam ends with $\vec{F}_{\mathrm{spec}} = \vec{M}_{\mathrm{spec}} = 0$, such as at a wingtip, and also in the interior at beam-joint or ground locations where displacement and load compatibility conditions between the joined beams are imposed.

Local Dynamics and Applied Loads

From Figure 3, the absolute velocity $\vec{v}$ and acceleration $\vec{a}$ at a beam point $\vec{r}_i$ on the s-axis have the following forms. Centripetal and Coriolis terms appear in $\vec{a}_i$.

$$\begin{aligned} \vec{v}(\vec{r}_i) \equiv \vec{v}_i &= \vec{U} + \vec{u}_i + \vec{\Omega} \times \vec{r}_i \\ \vec{a}(\vec{r}_i) \equiv \vec{a}_i &= \dot{\vec{U}} + \dot{\vec{u}}_i + \dot{\vec{\Omega}} \times \vec{r}_i \\ &+ \vec{\Omega} \times \left(\vec{\Omega} \times \vec{r}_i\right) + 2\vec{\Omega} \times \vec{u}_i \end{aligned}$$

A beam point $\vec{r}_p$ off of the s-axis is defined by an offset vector $\Delta\vec{r}_p$, fixed to the local csn system. Its relative rate is then due only to its relative rotation $\vec{\omega}_i$.

$$\frac{d}{dt}\Delta\vec{r}_p = \vec{\omega}_i \times \Delta\vec{r}_p$$

4

The absolute velocity and acceleration at $\vec{r}_p$ follow.

$$\vec{r}_p = \vec{r}_i + \Delta\vec{r}_p$$

$$\vec{v}(\vec{r}_p) \equiv \vec{v}_p = \vec{v}_i + \left(\vec{\Omega}+\vec{\omega}_i\right)\times\Delta\vec{r}_p \quad (12)$$

$$\vec{a}(\vec{r}_p) \equiv \vec{a}_p = \vec{a}_i + \left(\dot{\vec{\Omega}}+\dot{\vec{\omega}}_i\right)\times\Delta\vec{r}_p$$
$$+ \vec{\Omega}\times\left(\vec{\Omega}\times\Delta\vec{r}_p\right)$$
$$+ \left(2\vec{\Omega}+\vec{\omega}_i\right)\times(\vec{\omega}_i\times\Delta\vec{r}_p) \quad (13)$$

The total applied distributed loads consist of lift, drag, acceleration, and apparent-mass forces.

$$\vec{f} = \vec{f}_{\text{lift}} + \vec{f}_{\text{drag}} + \vec{f}_{\text{acc}} + \vec{f}_{\text{am}}$$
$$\vec{m} = \vec{m}_{\text{lift}} + \vec{m}_{\text{drag}} + \vec{m}_{\text{acc}} + \vec{m}_{\text{am}}$$

The applied concentrated loads are due to point masses, external elastic struts, and beam joints.

$$\Delta\vec{F}_P = \Delta\vec{F}_{\text{pm}} + \Delta\vec{F}_{\text{strut}} + \Delta\vec{F}_{\text{joint}}$$
$$\Delta\vec{M}_P = \Delta\vec{M}_{\text{pm}} + \Delta\vec{M}_{\text{strut}} + \Delta\vec{M}_{\text{joint}}$$

All loads will involve the local $\hat{c}, \hat{s}, \hat{n}$ unit vectors, shown in Figure 3. When specified in xyz axes, they are simply the rows of the transformation tensor.

$$\begin{bmatrix} \cdots\hat{c}\cdots \\ \cdots\hat{s}\cdots \\ \cdots\hat{n}\cdots \end{bmatrix}_{xyz} = \begin{bmatrix} \quad \bar{\bar{T}} \quad \end{bmatrix}$$

Aerodynamic Loads

Unsteady aerodynamic loads are given in terms of an unsteady circulation Γ on the lifting-line beams and trailing vortex sheets, expanded in a time-lagged Fourier series in the spanwise Glauert angle θ.

$$\Gamma(\theta,\tau) = \sum_{k=1}^{K} A_k(\tau)\sin(k\theta) \quad (14)$$

$$\theta = \arccos(s/s_{\max}) \quad , \quad \tau = t - \ell/V_\infty$$

Here, $-s_{\max}\le s\le s_{\max}$ is the spanwise arc length, and ℓ is the streamwise arc length. Alternatively, a simpler piecewise-constant spanwise distribution $A_i(\tau)$ can be employed, but at some cost increase. The circulation $\Gamma(\theta,t)$ on the beam itself corresponds to $\ell = 0$.

Velocity Summation. The absolute velocity $\vec{v}_{c/4}$ of the bound vortex at the quarter-chord location $\vec{r}_{c/4}$ is given by equation (12).

$$\Delta\vec{r}_{c/4} = (\bar{c}/4 - \bar{x}_o)\,\hat{c}$$
$$\vec{v}_{c/4} = \vec{v}_i + \left(\vec{\Omega}+\vec{\omega}_i\right)\times\Delta\vec{r}_{c/4}$$

The velocity relative to the bound vortex is then given by a kinematic velocity summation.

$$\vec{V}(\vec{r}_{c/4},t) = \vec{V}_{\text{ind}} + \Delta\vec{V}_{\text{gust}} - \vec{v}_{c/4}$$
$$\vec{V}_{\text{ind}} = \sum_{k=1}^{K} \vec{w}_k(\vec{r}_{c/4},t)\,A_k + \vec{w}_\infty(\vec{r}_{c/4})\,V_\infty$$

The $\vec{w}$ influence functions for the induced velocity will be developed later.

The gust velocity is prescribed as a function of position $\vec{R}_E$, with $(\ )_E$ denoting reference to earth XYZ axes. Conversion into the xyz axes is via the $\bar{\bar{T}}_E$ transformation tensor, formed using the Φ,Θ,Ψ aircraft Euler angle sequence pictured in Figure 2.

$$\vec{r}_E = \vec{R}_E + \bar{\bar{T}}_E\,\vec{r}$$
$$\Delta\vec{V}_{\text{gust}}(\vec{r};\vec{R}_E,\vec{\Theta}) = \bar{\bar{T}}_E^T\,\vec{V}_{E_{\text{gust}}}(\vec{r}_E)$$

Surface-beam lift and drag forces. The lift and moment are determined using the steady and unsteady vector form of the Kutta-Joukowsky theorem, with the relative velocity $\vec{V}$ taken at $\vec{r}_{c/4}$.

$$\vec{f}_{\text{lift}} = \rho\,\Gamma\,\vec{V}\times\hat{s} + \rho\,\frac{\partial\Gamma}{\partial t}\,\frac{\bar{c}}{|\vec{V}_\perp|}\,\vec{V}\times\hat{s} \quad (15)$$

$$\vec{m}_{\text{lift}} = \Delta\vec{r}_{c/4}\times\vec{f}_{\text{lift}} + \frac{1}{2}\rho\,|\vec{V}_\perp|^2\,\bar{c}^2\,c_m\,\hat{s} \quad (16)$$

$$\vec{V}_\perp = \vec{V} - (\vec{V}\cdot\hat{s})\,\hat{s}$$

With a suitable constraint on Γ, these forms will be seen to closely reproduce Theodorsen's result[5] in the 2D case. The pitching moment coefficient is given by

$$c_m = \left(c_{m_o} + \frac{dc_m}{d\delta_{F_1}}\delta_{F_1} + \frac{dc_m}{d\delta_{F_2}}\delta_{F_2}\cdots\right)\frac{1}{\sqrt{1-M_\perp^2}}$$

and has contributions from control surface or flap deflections δ_F. These terms allow modeling of effects such as aileron reversal. The Prandtl-Glauert factor uses the local perpendicular Mach number $M_\perp = |\vec{V}_\perp|/V_{\text{sound}}$.

The profile drag force is resolved into a friction-drag part along $\vec{V}$, and a pressure-drag part perpendicular to the beam's axis. The profile-drag moment is neglected.

$$\vec{f}_{\text{drag}} = \frac{1}{2}\rho\,|\vec{V}|\vec{V}\,\bar{c}\,c_{d_f} + \frac{1}{2}\rho\,|\vec{V}_\perp|\vec{V}_\perp\,\bar{c}\,c_{d_p} \quad (17)$$

$$+ 2\rho\,\frac{\vec{V}_\perp}{|\vec{V}_\perp|}\left(\vec{V}_{c.p.}\cdot\hat{n}_{c.p.}\right)^2\bar{c} \quad (18)$$

The third term is nonzero only when the local c_ℓ exceeds the stall limits, as will be described later.

5

Fuselage-beam lift and drag forces. The lift force on a fuselage beam of radius R is determined from slender-body theory.

$$\begin{aligned}
\vec{f}_{\text{lift}} &= \rho\,\vec{V}_\perp\,(\vec{V}\cdot\hat{s})\,2\pi R\frac{dR}{ds}\\
\vec{f}_{\text{drag}} &= \frac{1}{2}\rho\,|\vec{V}|\,\vec{V}\,2R\,c_{d_f}\ +\ \frac{1}{2}\rho\,|\vec{V}_\perp|\,\vec{V}_\perp\,2R\,c_{d_p}
\end{aligned}$$

Here, c_{d_f} is comparable to the skin C_f, and c_{d_p} corresponds to the C_D of a circular cylinder, roughly 1.2 for subcritical flow, and 0.4 for supercritical flow.

Inertial and Gravity Loads

The inertia and gravity loads act at the local mass centroid $\vec{r}_i + \Delta\vec{r}_{cg}$. From equation (13)

$$\begin{aligned}
\Delta\vec{r}_{cg} &= c_{cg}\,\hat{c}\ +\ n_{cg}\,\hat{n}\\
\vec{a}_{cg} &= \vec{a}_i\ +\ \left(\dot{\vec{\Omega}}+\dot{\vec{\omega}}_i\right)\times\Delta\vec{r}_{cg}\\
&\quad +\ \vec{\Omega}\times\left(\vec{\Omega}\times\Delta\vec{r}_{cg}\right)+\left(2\vec{\Omega}+\vec{\omega}_i\right)\times(\vec{\omega}_i\times\Delta\vec{r}_{cg})
\end{aligned}$$

and the gravity, inertial, and precession loads are

$$\begin{aligned}
\vec{f}_{\text{acc}} &= \mu\,(\vec{g}-\vec{a}_{cg})\\
\vec{m}_{\text{acc}} &= \Delta\vec{r}_{cg}\times\vec{f}_{\text{acc}}\ -\ \bar{\bar{T}}^T\,\bar{\bar{\iota}}\,\bar{\bar{T}}\left(\dot{\vec{\Omega}}+\dot{\vec{\omega}}_i\right)\\
&\quad -\ \left(\vec{\Omega}+\vec{\omega}_i\right)\times\left\{\bar{\bar{T}}^T\,\bar{\bar{\iota}}\,\bar{\bar{T}}\left(\vec{\Omega}+\vec{\omega}_i\right)\right\}
\end{aligned}$$

where μ is the mass/length density of the beam, and $\bar{\bar{\iota}}$ is the section inertia/length tensor in csn axes.

The apparent-mass loads can depend only on the normal component of the acceleration $\vec{a}_{c/2}$.

$$\begin{aligned}
\Delta\vec{r}_{c/2} &= (\bar{c}/2-\bar{x}_o)\,\hat{c}\\
\vec{a}_{c/2} &= \vec{a}_i\ +\ \left(\dot{\vec{\Omega}}+\dot{\vec{\omega}}_i\right)\times\Delta\vec{r}_{c/2}\\
&\quad +\ \vec{\Omega}\times\left(\vec{\Omega}\times\Delta\vec{r}_{c/2}\right)+\left(2\vec{\Omega}+\vec{\omega}_i\right)\times(\vec{\omega}_i\times\Delta\vec{r}_{c/2})
\end{aligned}$$

The force and moment follow from Theodorsen's theory.

$$\begin{aligned}
\vec{f}_{\text{am}} &= \frac{\pi}{4}\rho\,\bar{c}^2\left[\vec{V}\times\left(\vec{\Omega}+\vec{\omega}_i\right)\cdot\hat{n}\ -\ \vec{a}_{c/2}\cdot\hat{n}\right]\hat{n}\\
\vec{m}_{\text{am}} &= -\frac{\pi}{16}\rho\,\bar{c}^3\left[\vec{V}\times\left(\vec{\Omega}+\vec{\omega}_i\right)\cdot\hat{n}\ +\ \frac{\bar{c}}{8}\left(\dot{\vec{\Omega}}+\dot{\vec{\omega}}_i\right)\cdot\hat{s}\right]\hat{s}\\
&\quad +\ \Delta\vec{r}_{c/2}\times\vec{f}_{\text{am}}
\end{aligned}$$

The apparent-mass loads on a fuselage beam are determined via slender-body theory.

$$\vec{f}_{\text{am}} = -2\pi\,\rho\,R^2\left(\vec{a}_i-(\vec{a}_i\cdot\hat{s})\,\hat{s}\right)$$

Point-Mass Loads

A point with mass m_p and angular momentum $\vec{H}_p$ can represent a nacelle, external store, rotor, etc, mounted to a beam by a rigid pylon, as shown in Figure 6. Its location and angular momentum in xyz axes are:

$$\begin{aligned}
\Delta\vec{r}_p &= \bar{\bar{T}}^T\left\{c_p\ s_p\ n_p\right\}^T\ =\ \bar{\bar{T}}^T\,\bar{\bar{T}}_0\,\Delta\vec{r}_{p_0}\\
\vec{r}_p &= \vec{r}_i\ +\ \Delta\vec{r}_p\\
\vec{H}_p &= \bar{\bar{T}}^T\,\bar{\bar{T}}_0\,\vec{H}_{p_0}
\end{aligned}$$

Although $\bar{\bar{T}}_0$, $\Delta\vec{r}_{p_0}$, $\vec{H}_{p_0}$ are fixed at their jig values, $\vec{r}_p$ and $\vec{H}_p$ are "waved around" appropriately in space along with the beam.
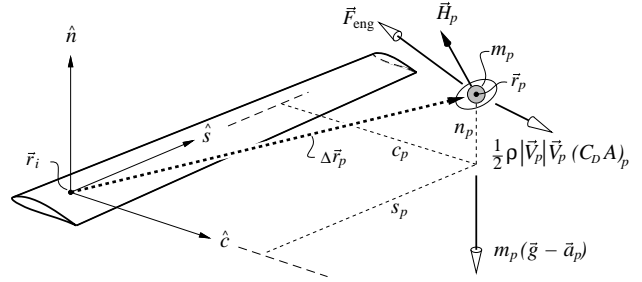
Fig. 6 Point mass m_p with angular momentum $\vec{H}_p$ and applied loads, cantilevered by rigid pylon.

The force and moment applied to the beam are

$$\begin{aligned}
\Delta\vec{F}_{\text{pm}} &= m_p(\vec{g}-\vec{a}_p)+\frac{1}{2}\rho\,|\vec{V}_p|\,\vec{V}_p\,(C_DA)_p+\vec{F}_{\text{eng}}\\
\Delta\vec{M}_{\text{pm}} &= \Delta\vec{r}_p\times\Delta\vec{F}_{\text{pm}}-\left(\vec{\Omega}+\vec{\omega}_i\right)\times\vec{H}_p+\vec{M}_{\text{eng}}
\end{aligned}$$

where $\vec{V}_p$ and $\vec{a}_p$ are defined from $\Delta\vec{r}_p$ via relations (12,13). Including the "engine" loads $\vec{F}_{\text{eng}},\vec{M}_{\text{eng}}$ allows the point to represent a thrusting engine nacelle.

Joint Loads

A *joint* is a rigid pylon linking $\vec{r}_1$ and $\vec{r}_2$ on the joined beams, as sketched in Figure 7.

The displacements and loads of the pylon $\Delta\vec{r}_J$, $\Delta\vec{\theta}_J$, $\vec{F}_J$, $\vec{M}_J$, define loads and kinematic constraints on the joined beams. The pylon applies point loads to the beam at point #1, and sets kinematic constraints at point #2.

$$\Delta\vec{F}_{\text{joint}} = \vec{F}_J\quad,\quad \Delta\vec{M}_{\text{joint}} = \vec{M}_J\quad(\#1)\ (19)$$
$$\vec{r}_i = \vec{r}_{0_i}+\Delta\vec{r}_J\quad,\quad \vec{\theta}_i = \vec{\theta}_{0_i}+\Delta\vec{\theta}_J\quad(\#2)\ (20)$$

Conditions (20) replace the equilibrium equations (8,9). These "lost" equations are imposed separately as constraints effectively determining $\vec{M}_J$ and $\vec{F}_J$.
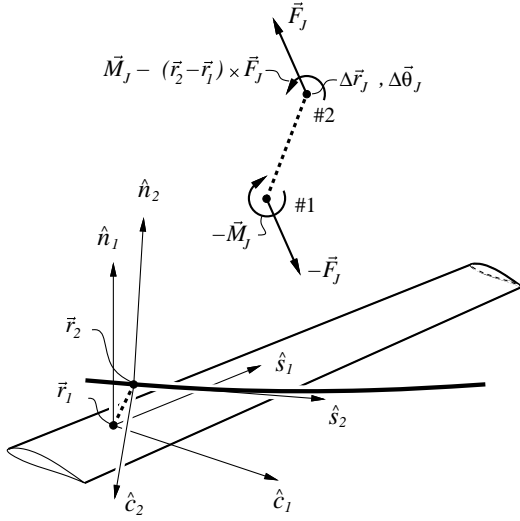
Fig. 7 A joint pylon linking two beams.

Velocity Influence Coefficients

Prandtl-Glauert Transformation

The induced velocity has contributions from vorticity on the lifting surface beams and trailing vortex sheets, and from source and doublet distributions along the beams with volume. Figure 8 shows the quantities involved in the relevant summation integrals, performed in the wind-aligned Prandtl-Glauert space $\{\xi, \eta, \zeta\}^T = \bar{\bar{P}} \{x, y, z\}^T$ to account for compressibility.

$$\bar{\bar{P}} = \begin{bmatrix} \cdots \vec{\xi} \cdots \\ \cdots \hat{\eta} \cdots \\ \cdots \hat{\zeta} \cdots \end{bmatrix} = \begin{bmatrix} \frac{1}{\lambda} \cos\alpha \cos\beta & -\frac{1}{\lambda} \sin\beta & \frac{1}{\lambda} \sin\alpha \cos\beta \\ \cos\alpha \sin\beta & \cos\beta & \sin\alpha \sin\beta \\ -\sin\alpha & 0 & \cos\alpha \end{bmatrix}$$

The $\vec{\xi}$ vector is aligned with $\vec{V}_\infty$ as can be seen by comparing with equation (1).

The PG equation for the perturbation potential $\phi(x, y, z)$ transforms to the Laplace equation in $\xi\eta\zeta$ space, whose solution for unit A_k and V_∞ gives the influence functions $\vec{w}_k$ and $\vec{w}_\infty$. The summation integrals effectively give the $\xi\eta\zeta$-velocity $\nabla_{\xi\eta\zeta} \phi$. The xyz-velocity is then obtained via the chain rule, which amounts to multiplication by the transpose of $\bar{\bar{P}}$ (not its inverse).

$$\vec{V}_{\text{ind}} = \nabla_{xyz} \phi = \bar{\bar{P}}^T \nabla_{\xi\eta\zeta} \phi \qquad (21)$$

Vortex Influence Function

The vortex influence function $\vec{w}_k(\vec{r})$ is given by the Biot-Savart integral over the k'th circulation mode. The mode's vorticity is represented by a discrete bound/trailing vortex lattice system, shown in Figure 9.
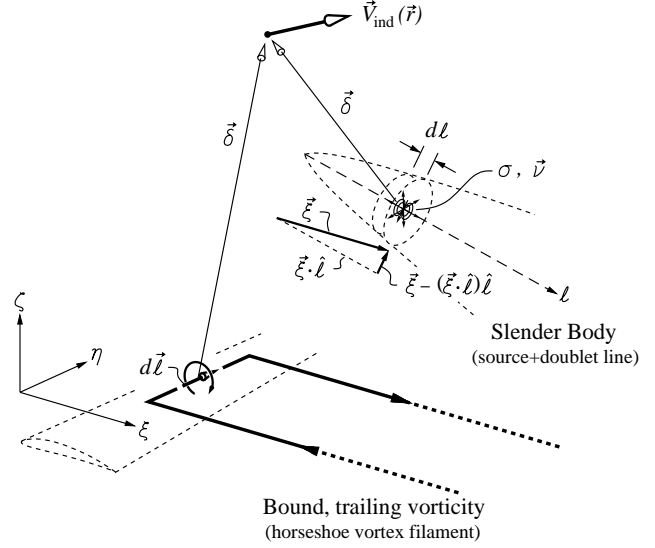

Fig. 8 Induced velocity contributions from, vortex, source, and doublet distributions.
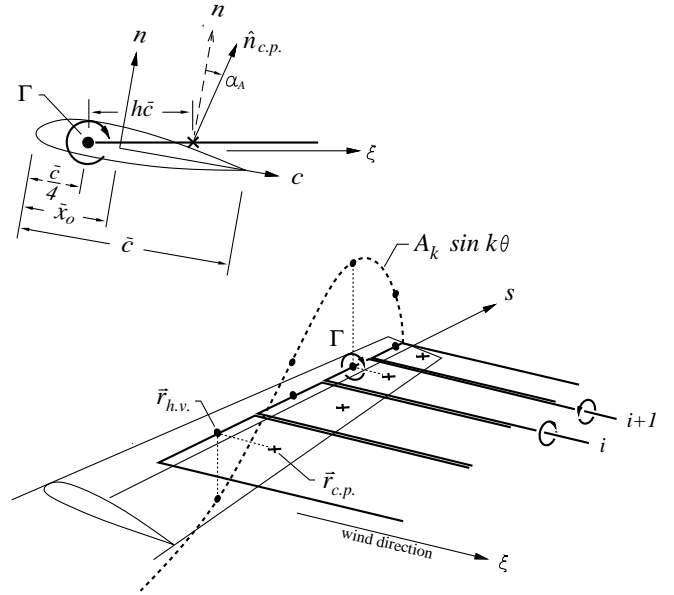

Fig. 9 Airfoil-plane dimensions, and circulation mode represented by horseshoe vortices.

The location of the bound vortex segment midpoint $\vec{r}_{h.v.}$ is at the quarter-chord point along the ξ axis,

$$\vec{r}_{h.v.} = \vec{r}_a + \frac{\bar{c}/4 - \bar{x}_o}{|\vec{\xi} \times \hat{s}|} \vec{\xi}$$

The control point $\vec{r}_{c.p.}$ is directly "downstream"

$$\vec{r}_{c.p.} = \vec{r}_{h.v.} + \frac{h \bar{c}_a}{|\vec{\xi} \times \hat{s}|} \vec{\xi}$$

where h is chosen so that the local incompressible 2-D

7

section lift-curve slope is reproduced.

$$h = \frac{1}{4\pi}\frac{dc_\ell}{d\alpha}$$

For thin airfoils, $h = 1/2$ is appropriate. Both $\vec{r}_{h.v.}$ and $\vec{r}_{c.p.}$ shift spanwise as the freestream direction changes.

The effective normal vector $\hat{n}_{c.p.}$ at the control point is rotated away from the geometric $\hat{n}$ by the zero-lift line angle α_A relative to the c axis. This includes contributions from the flap deflections δ_F.

$$\hat{n}_{c.p.} = \bar{\bar{T}}^T \{\sin\alpha_A \quad 0 \quad \cos\alpha_A\}^T$$

$$\alpha_A = \alpha_{A_o} + \frac{dc_\ell/d\delta_{F_1}}{dc_\ell/d\alpha}\delta_{F_1} + \frac{dc_\ell/d\delta_{F_2}}{dc_\ell/d\alpha}\delta_{F_2}\cdots$$

The overall $\vec{w}_k$ for the k'th mode $\sin(k\theta)$ is given by the Biot-Savart law applied to the mode's vortices.

$$\vec{w}_k = \bar{\bar{P}}^T\nabla_{\xi\eta\zeta}\phi_k = \left[\ \bar{\bar{P}}^T\ \right]\left\{\frac{1}{4\pi}\sum_{i=1}^{I-1}\sin(k\theta_a)\int\frac{d\vec{\ell}\times\vec{\delta}}{\delta^3}\right\}$$

The vortex element $d\vec{\ell}$ belongs to the horseshoe vortex spanning the $i...i+1$ stations, and $\vec{\delta}$ is the relative position of the field point, as shown in Figure 8. Both are defined in $\xi\eta\zeta$ space.

$$d\vec{\ell} = \bar{\bar{P}}\,d\vec{r} \qquad\qquad \vec{\delta} = \bar{\bar{P}}\{\vec{r}-\vec{r}_{(\ell)}\}$$

For surfaces which do not contain the control point in question, $\vec{w}_k$ is modified by a finite vortex core size ε, by replacing $\delta^2 \to \delta^2 + \varepsilon^2$. Choosing $\varepsilon = \max(\bar{c}_a/4,\,\Delta s)$ results in the vortex filaments being smeared into a continuous vortex sheet. This is essential to produce a well-behaved solution if the wake impinges on a downstream surface.

For unsteady flows, The Biot-Savart integral above is also evaluated for the shed vortices, whose strength is obtained from $A_k(\tau)$'s dependence on ℓ via the lagged-time variable τ. No attempt is currently made to track the trajectories of the shed vortices. The entire wake geometry is simply assumed to be straight, and aligned with the instantaneous $\vec{V}_\infty$.

Locally-2D Approximation

In lieu of computing the shed vortices' contribution to $\vec{w}_k$ at control points $\vec{r}_{c.p.}$, a simpler and more economical approach is to integrate only over the "steady" bound and trailing vortices, and to model the shed vortices by an empirical lag term.

$$(\vec{V}_{\text{ind}})_{c.p.} = \sum_{k=1}^{K}\vec{w}_k A_k(t) + \vec{w}_\infty V_\infty(t) - \frac{b}{V_\perp}\frac{\partial\Gamma}{\partial t}\hat{n}_{c.p.} \quad (22)$$

The last lag term accounts for the downwash of the local spanwise vorticity being shed at a rate of $\partial\Gamma/\partial t$.

In the 2D thin-airfoil limit, using $(\vec{V}_{\text{ind}})_{c.p.}$ above to set flow tangency at the 3/4 chord point gives

$$\Gamma + \pi\bar{c}\frac{b}{V}\frac{d\Gamma}{dt} = \pi\bar{c}\left[V\vartheta - \dot{z} + \frac{\bar{c}}{4}\dot{\vartheta}\right] \quad (23)$$

where $\vartheta(t)$ and $z(t)$ are the pitch and plunge motions. For harmonic motion,

$$\vartheta(t) = \tilde{\vartheta}e^{i\omega t}\ ,\quad z(t) = \tilde{z}e^{i\omega t}\ ,\quad \Gamma(t) = \tilde{\Gamma}e^{i\omega t}$$

and the circulation-related lift follows from (15),

$$\tilde{f}_{\text{lift}} = \rho V\tilde{\Gamma}\,(1+2ik)$$
$$= \pi\rho V^2\,\bar{c}\left[\left(1+\frac{ik}{2}\right)\tilde{\vartheta} - \frac{ik\tilde{z}}{\bar{c}/2}\right]\frac{1+2ik}{1+2\pi ik\,b} \quad (24)$$

with $k = \omega\bar{c}/2V$. To match Theodorsen's result, the fraction on the righthand side *should* be equal to the Theodorsen lag function $C(k) = F(k) + iG(k)$, which has $C(k) \to 1/2$ asymptotically as $k \to \infty$. Setting $b = 2/\pi$ to match this limit defines an implied effective lag function.

$$C_{\text{implied}}(k) = (F+iG)_{\text{implied}} = \frac{1+2ik}{1+4ik} \quad (25)$$

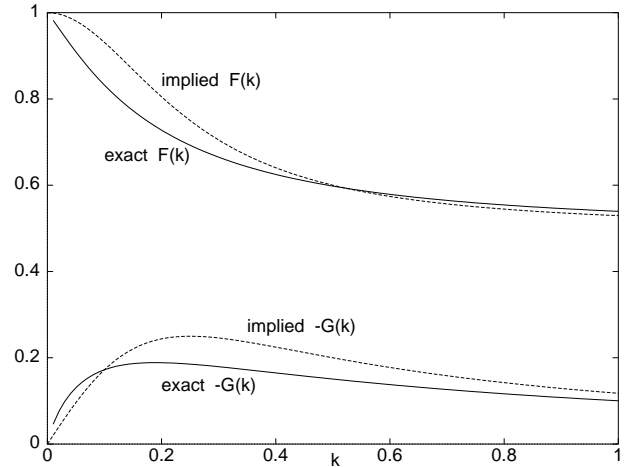Figure 10 shows that the two compare reasonably well.

Fig. 10   Exact Theodorsen function, compared to approximation implied by lagged downwash in (22)

Volume Influence Functions

The volume contribution to the induced velocity is given by source and doublet densities σ, $\vec{\nu}$. These give flow tangency on the circular beam of cross-sectional area πR^2, in the presence of unit freestream $\vec{\xi}$,

$$\sigma(\ell) = \frac{d(\pi R^2)}{d\ell}\left(\vec{\xi}\cdot\hat{\ell}\right)\ ,\quad \vec{\nu}(\ell) = 2\pi R^2\left(\vec{\xi}-(\vec{\xi}\cdot\hat{\ell})\hat{\ell}\right)$$

8

and are defined in $\xi\eta\zeta$ space. Integration along all beams gives the volume influence function.

$$\vec{w}_\infty(\vec{r}) = \begin{bmatrix} \bar{\bar{P}}^T \end{bmatrix} \left\{ \frac{1}{4\pi} \int \left[\frac{\sigma\vec{\delta}}{(\delta^2 + \varepsilon^2)^{3/2}} \right. \right.$$
$$\left. \left. + \frac{\vec{\nu}\delta^2 - 3(\vec{\nu}\cdot\vec{\delta})\,\vec{\delta}}{(\delta^2 + \varepsilon^2)^{5/2}} \right] d\ell \right\} \quad (26)$$

A suitable desingularizing "core size" is $\varepsilon = R/2$.

Global Variables and Constraints

In addition to the 18 structural node unknowns $x_i, y_i, \dots$ listed earlier, the overall aero/structural problem also has a smaller number of "global" variables

$$\Delta\vec{r}_J \quad \Delta\vec{\theta}_J \quad \vec{F}_J \quad \vec{M}_J \quad A_k \quad \vec{R}_E \quad \vec{\Theta} \quad \vec{U} \quad \dot{\vec{U}} \quad \vec{\Omega} \quad \dot{\vec{\Omega}} \quad \delta_{F_1} \quad \delta_{F_2} \dots$$

which require the same number of constraints.

Aircraft-Motion Constraints

The aircraft position $\vec{R}_E$ and Euler angles $\vec{\Theta}$ are constrained by direct kinematic relations.

$$\frac{d}{dt}\vec{R}_E - \bar{\bar{T}}_E\,\vec{U} = 0$$
$$\frac{d}{dt}\vec{\Theta} - \left[\bar{\bar{T}}_E^T\,\bar{\bar{K}}_E\right]^{-1}\vec{\Omega} = 0$$

Velocity and Rotation-Rate Constraints

For static cases, the aircraft velocity $\vec{U}$ can be constrained directly, typically with specified V_∞, α, β in equation (1). The angular rates $\vec{\Omega}$ can also be constrained directly, or indirectly by specifying a zero moments about a chosen reference point. The latter option can be used to determine trimmed-flight steady rotation rates, for example.

For unsteady flight cases, $\vec{U}$ and $\vec{\Omega}$ are governed by their kinematic constraints.

$$\frac{d}{dt}\vec{U} - \dot{\vec{U}} + \vec{\Omega}\times\vec{U} = 0 \quad , \qquad \frac{d}{dt}\vec{\Omega} - \dot{\vec{\Omega}} = 0$$

Acceleration Constraints

The accelerations $\dot{\vec{U}}$, $\dot{\vec{\Omega}}$ can be constrained directly,

$$\dot{\vec{U}} = \dot{\vec{U}}_{\text{spec}} \quad , \qquad \dot{\vec{\Omega}} = \dot{\vec{\Omega}}_{\text{spec}}$$

which simulates a zero or prescribed motion. For quasi-static flight, it is necessary to impose overall force and moment balance instead. The appropriate equations are

$$\vec{F}_{i+1} - \vec{F}_i = 0 \quad , \qquad \vec{M}_{i+1} - \vec{M}_i = 0$$

imposed across the zero-length ground interval.

Beam Joint Constraints

Twelve constraints are required for $\Delta\vec{r}_J, \Delta\vec{\theta}_J, \vec{M}_J, \vec{F}_J$ defined for each beam joint, shown in Figure 7. Setting

$$\vec{r}_2 - \vec{r}_1 - \bar{\bar{T}}_1^T\,\bar{\bar{T}}_{1_0}\,(\vec{r}_{2_0} - \vec{r}_{1_0}) = 0$$
$$\left[\bar{\bar{T}}_1^T\,\bar{\bar{T}}_{1_0}\right] \otimes \left[\bar{\bar{T}}_2^T\,\bar{\bar{T}}_{2_0}\right] = 0$$

forces the joined beams to retain their unloaded-state distance and relative orientation. The other six are load equilibrium equations (8,9), with added joint loads. These were displaced by kinematic constraints (20).

$$\Delta\vec{M} + \vec{m}_a\,\Delta s + \Delta\vec{r}\times\vec{F}_a = \vec{M}_J - (\vec{r}_{i_2} - \vec{r}_{i_1})\times\vec{F}_J$$
$$\Delta\vec{F} + \vec{f}_a\,\Delta s = \vec{F}_J$$

Circulation Coefficient Constraints

The circulation coefficients A_k for each surface require constraints which enforce flow tangency on that surface.

$$\vec{V}_{c.p.} \cdot \hat{n}_{c.p.} = 0 \quad (27)$$

If the locally-2D unsteady approximation is used (22), a slightly modified flow-tangency constraint results.

$$\left(\vec{V}\cdot\hat{n}\right)_{\text{net}} \equiv \left(\vec{V}_{c.p.}\cdot\hat{n}_{c.p.}\right) - \frac{b}{V_\perp}\frac{\partial\Gamma}{\partial t} = 0 \quad (28)$$

In either case, typically fewer circulation coefficients $A_{1\dots K}$ are present than control points $1\dots I-1$. A weighted-residual approach is therefore used.

$$\sum_{i=1}^{I-1} \left(\vec{V}_{c.p.}\cdot\hat{n}_{c.p.}\right)_a \, \sin(k\theta_a)\,\Delta\theta = 0 \quad ; \quad k = 1\dots K$$

In effect, a discrete Fourier analysis of the flow tangency residual is performed for each surface, with the K lowest residual wavenumbers being required to vanish.

The flow tangency requirement (27) or (28) is modified to model stall, using the local lift coefficient:

$$\vec{V}(\vec{r}_{c.p.})\cdot\hat{n}_{c.p.} - \frac{V_\perp}{4\pi h}K_s\,f_{\text{stall}}(c_\ell) = 0 \quad (29)$$

$$c_\ell = 2\Gamma/\bar{c}V_\perp$$
$$f_{\text{stall}}(c_\ell) = \Delta c_\ell \log\frac{1 + \exp[(c_\ell - c_{\ell\max})/\Delta c_\ell]}{1 + \exp[(c_{\ell\min} - c_\ell)/\Delta c_\ell]}$$

where the f_{stall} function has a derivative of zero inside the stall limits, and unity outside the stall limits. In the 2D case this gives a lift curve slope of

$$\frac{dc_\ell}{d\alpha} \simeq \begin{cases} 4\pi h & , \quad c_{\ell\min} < c_\ell < c_{\ell\max} \\ 4\pi h/(1 + K_s) & , \quad c_\ell < c_{\ell\min} \quad , \quad c_{\ell\max} < c_\ell \end{cases}$$

inside and outside the stall limits, as sketched in Figure 11. The width of the stall transition region is roughly Δc_ℓ. Using $K_s \simeq 40$ and $\Delta c_\ell \simeq 0.05$ gives a realistic 2D $c_\ell(\alpha)$ lift curve. The nonzero post-stall $\vec{V} \cdot \hat{n}$ implied by equation (29) results in a drag-force contribution in (18). This added profile drag coefficient is

$$c_d \; = \; 4 \left(\frac{\vec{V} \cdot \hat{n}}{V} \right)^2 \; \simeq \; 4 \left(\frac{K_s}{1+K_s} \right)^2 \left(\sin \alpha \, - \, \frac{c_{\ell \max}}{4\pi h} \right)^2$$

and reaches approximately $c_d \simeq 2.0$ at $\alpha = 90°$.
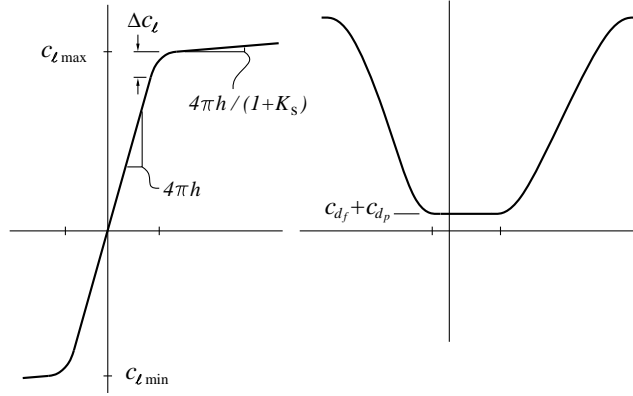
Fig. 11   Effective section $c_\ell(\alpha)$ and $c_d(\alpha)$ resulting from stall model.

Newton System Structure

The state defining the overall unsteady problem is conveniently partitioned into two vectors.

$$\mathbf{U} \;\; = \;\; \left(\vec{r}_i \;\;\; \vec{\theta}_i \;\;\; \vec{M}_i \;\;\; \vec{F}_i \;\;\; \vec{u}_i \;\;\; \vec{\omega}_i \;\;\;\; \Delta\vec{r}_J \;\;\; \Delta\vec{\theta}_J \;\;\; \vec{M}_J \;\;\; \vec{F}_J \right.$$
$$\left. A_k \;\;\; \vec{R}_E \;\;\; \vec{\Theta} \;\;\; \vec{U} \;\;\; \vec{\Omega} \;\;\; \dot{\vec{U}} \;\;\; \dot{\vec{\Omega}} \;\;\; \mathbf{E} \right)$$
$$\mathbf{D} \;\; = \;\; \left(\delta_{F\,1} \;\;\; \delta_{F\,2} \ldots \right)$$

Here, $\mathbf{E}$ is a control error-integral vector defined as

$$\mathbf{E} \; = \; \int^t (\mathbf{U} - \mathbf{U}_c) \, dt \quad \text{or} \quad \dot{\mathbf{E}} \; = \; \mathbf{U} - \mathbf{U}_c$$

where $\mathbf{U}_c$ is the commanded state. Typically, $\mathbf{E}$ and $\mathbf{U}_c$ have only a few nonzero elements, although simulation of full-state control is computationally feasible here.

All equations are treated in nonlinear residual form

$$\mathbf{R}(\mathbf{U}, \dot{\mathbf{U}}, \mathbf{D} \,;\, \mathbf{U}_c) \; = \; \mathbf{0}$$

from which follows the corresponding linearized system.

$$\left[\frac{\partial \mathbf{R}}{\partial \mathbf{U}} \right] \delta\mathbf{U} + \left[\frac{\partial \mathbf{R}}{\partial \dot{\mathbf{U}}} \right] \delta\dot{\mathbf{U}} + \left[\frac{\partial \mathbf{R}}{\partial \mathbf{D}} \right] \delta\mathbf{D} \; = \; \delta\mathbf{R} \quad (30)$$

The leftmost Jacobian matrix has full rank. When the two other matrix terms are either eliminated or the equation system is suitably augmented, and $\delta\mathbf{R} = -\mathbf{R}$ is imposed, equation (30) becomes a Newton system which can be solved for the update vector $\delta\mathbf{U}$.

The most general constraints on $\mathbf{D}$ are some linear or nonlinear state-feedback control law residuals.

$$\mathbf{C}(\mathbf{U}, \dot{\mathbf{U}}, \mathbf{D} \,;\, \mathbf{U}_c) \; = \; \mathbf{0}$$

An explicit and more typical control law would be

$$\mathbf{C} \; \equiv \; \mathbf{D} + \mathbf{f}(\mathbf{U}, \dot{\mathbf{U}} \,;\, \mathbf{U}_c) \; = \; \mathbf{0}$$

or simply $\mathbf{D} = -\mathbf{f}(\mathbf{U}_c)$ in the case of open-loop control. In either case, the linearized form is:

$$\left[\frac{\partial \mathbf{f}}{\partial \mathbf{U}} \right] \delta\mathbf{U} \; + \; \left[\frac{\partial \mathbf{f}}{\partial \dot{\mathbf{U}}} \right] \delta\dot{\mathbf{U}} \; + \; \delta\mathbf{D} \; = \; -(\mathbf{D} + \mathbf{f}) \quad (31)$$

A convenient implementation of (31) uses the control law $\mathbf{f}(\ldots)$ provided by the user as a black-box subroutine, which allows quick prototype testing of candidate control schemes for stability. The commanded vector $\mathbf{U}_c(t)$ is imposed interactively at runtime. This allows rapid investigation of forced-response behavior as well.

System Solution

Four types of solutions can be performed, as described below. All rely on the same Jacobian matrices of the nonlinear system $\mathbf{R} = \mathbf{0}$, but in different ways.

Steady Calculation

Setting $\dot{\mathbf{U}} = \mathbf{0}$ and $\delta\dot{\mathbf{U}} = \mathbf{0}$ in (30,31) and iterating the resulting Newton system produces a steady or quasi-steady nonlinear solution $\mathbf{U}, \mathbf{D}$.

Time-Domain Calculation

A time history is a sequence of states $\mathbf{U}^1, \mathbf{U}^2 \ldots \mathbf{U}^n$ at specified times, with $\dot{\mathbf{U}}$ expressed as a backward difference in time, e.g.

$$\dot{\mathbf{U}} \; = \; k_0 \, \mathbf{U}^n \; + \; k_1 \, \mathbf{U}^{n-1} \; + \; k_2 \, \mathbf{U}^{n-2}$$

The time-differencing coefficients k are known constants. Hence, $\delta\dot{\mathbf{U}} = k_0 \, \delta\mathbf{U}$, which allows the elimination of the unsteady Jacobian via the substitution

$$\left[\frac{\partial \mathbf{R}}{\partial \mathbf{U}} \right] \delta\mathbf{U} + \left[\frac{\partial \mathbf{R}}{\partial \dot{\mathbf{U}}} \right] \delta\dot{\mathbf{U}} \;\; \longrightarrow \;\; \left[\frac{\partial \mathbf{R}}{\partial \mathbf{U}} + k_0 \frac{\partial \mathbf{R}}{\partial \dot{\mathbf{U}}} \right] \delta\mathbf{U}$$

and likewise for $[\partial \mathbf{f}/\partial \mathbf{U}]$ and $[\partial \mathbf{f}/\partial \dot{\mathbf{U}}]$. The resulting Newton system (30,31) is iterated for the unknown $\mathbf{U}^n$, $\mathbf{D}^n$ at each time level.

Frequency-Response Analysis

A small time-harmonic state variation in the form

$$\delta \mathbf{U} = \hat{\mathbf{U}} \exp(i\omega t)$$

is superimposed on some converged steady or unsteady (time-marched) nonlinear state $\mathbf{U}$. The perturbed $\mathbf{U}$ must still satisfy $\mathbf{R}(\mathbf{U}, \dot{\mathbf{U}}; \mathbf{U}_c) = \mathbf{0}$, and also the equivalent linearized form $\delta \mathbf{R} = \mathbf{0}$. The latter gives

$$\bar{\bar{\mathbf{A}}}\,\delta\mathbf{U} - \bar{\bar{\mathbf{M}}}\,\delta\dot{\mathbf{U}} = \bar{\bar{\mathbf{B}}}\,\delta\mathbf{U}_c \qquad (32)$$

$$\bar{\bar{\mathbf{A}}} = \frac{\partial \mathbf{R}}{\partial \mathbf{U}} \qquad \bar{\bar{\mathbf{M}}} = -\frac{\partial \mathbf{R}}{\partial \dot{\mathbf{U}}} \qquad \bar{\bar{\mathbf{B}}} = -\frac{\partial \mathbf{R}}{\partial \mathbf{U}_c}$$

where the Jacobian matrices have been simply renamed as the "stiffness", "mass", and "control" matrices. For brevity, $\mathbf{U}$ now includes $\mathbf{D}$, and $\mathbf{R}$ now includes $\mathbf{C}$.

The response coefficient $\hat{\mathbf{U}}$ is obtained from the specified $\hat{\mathbf{U}}_c$ by directly solving the complex form of system (32).

$$\left[\bar{\bar{\mathbf{A}}} - i\omega\,\bar{\bar{\mathbf{M}}} \right] \hat{\mathbf{U}} = \bar{\bar{\mathbf{B}}}\,\hat{\mathbf{U}}_c \qquad (33)$$

Typically $\hat{\mathbf{U}}_c$ contains specified control vector variables $(\delta_F)_c$. Solving (33) for a range of ω produces Bode plots for all quantities of interest.

The response $\hat{\mathbf{U}}$ is examined as a perturbed solution

$$\mathbf{U}' = \Re\left\{ \mathbf{U} + c\,\hat{\mathbf{U}}\exp(i\phi) \right\}$$

with the scale c and phase ϕ provided at runtime. Alternatively, setting $\phi = \omega t$ generates an on-screen movie of $\mathbf{U}'(t)$. Both methods are useful.

Eigenmode Analysis

Eigenmodes are nontrivial solutions $\hat{\mathbf{X}}_\ell$ of the unforced system (33), with unknown complex eigenvalues λ_ℓ replacing the forcing imaginary frequency $i\omega$.

$$\bar{\bar{\mathbf{A}}}\,\hat{\mathbf{X}}_\ell = \bar{\bar{\mathbf{M}}}\,\hat{\mathbf{X}}_\ell\,\lambda_\ell \qquad (34)$$

Instability of eigenmode ℓ is indicated if $\Re(\lambda_\ell) > 0$. This can be either a flight instability (e.g. spiral), or a structural instability (e.g. flutter), as distinguished by the frequency $\Im(\lambda_\ell)$ and the structure of $\hat{\mathbf{X}}_\ell$.

The ARPACK[6] sparse eigenvalue package, based on Arnoldi iteration, is used to rapidly compute the eigenpairs from (34) during an interactive session.

Application Examples

Oscillating Beam

An eigenmode analysis is performed on a uniform beam floating freely in space to validate part of the method implementation and to test the accuracy of the finite-difference scheme. Table 1 shows the analytically-derived exact frequencies for the four lowest symmetric and antisymmetric modes. Also shown is the % error in the computed frequencies versus the number of grid nodes on one half of the beam. The error decreases as $(N-1)^{-2}$, confirming the method is 2nd-order accurate.

Table 1 Bending frequencies of free beam, and computed % error versus number of grid nodes N.

Mode	$\dfrac{\omega L^2}{\sqrt{EI/\mu}}$	$\left[\dfrac{\omega_{\mathrm{computed}}}{\omega_{\mathrm{exact}}} - 1\right] \times 100\%$			
	(exact)	$N=41$	$N=21$	$N=11$	$N=6$
1	5.5933	0.024	0.096	0.383	1.516
2	15.4182	0.090	0.360	1.443	5.805
3	30.2259	0.193	0.775	3.127	12.963
4	49.9649	0.336	1.350	5.513	23.829

2-D Flutter Case

A rigid wing of aspect ratio 200 is mounted on two massless "spring" beams with finite EA and GJ to duplicate the classical 2D bending/torsion flutter case analyzed by Theodorsen.[5] The intent is to validate much of the unsteady aerodynamic formulation, and to examine the limitations of the simple lagged-downwash approximation (22). The following parameters are chosen:

|	
Apparent-mass ratio:	$\pi\rho\bar{c}^2/4\mu = 0.2405$
Inertia/mass ratio:	$4\iota_{nn}/\mu\bar{c}^2 = 1.60$
Mass centroid:	$\bar{x}_{cg}/\bar{c} = 0.30\ldots0.50$

For this case flutter occurs at $k \simeq 0.2\ldots0.5$, depending on $\bar{x}_{cg}$. The rather large values of the apparent-mass and inertia ratios ensure that all the apparent mass and inertial-coupling terms in the beam loads $\vec{f}$ and $\vec{m}$ are active, giving a more thorough validation.

Figure 12 shows the flutter speeds computed in three ways: *i)* Theodorsen method with the "exact" $C(k)$ lag function, *ii)* Theodorsen method with the "implied" $C(k)$ lag function (25), *iii)* Present method, using the criterion $\Re(\lambda_\ell) = 0$ for the flutter onset, with λ_ℓ determined from an eigenvalue analysis of the entire system Jacobian as described in the previous section.

The near-exact agreement of *ii)* and *iii)* indicates that the overall aero/structural coupled formulation, and associated Jacobian and eigenvalue calculations are sound. The discrepancy between *i)* and *ii),iii)* is apparently due to the differences between C_{exact} and C_{implied} in Figure 10. In particular, F_{implied} and the resulting driving lift are somewhat too large in the k range involved here, and thus give an underpredicted V_{flutter}.
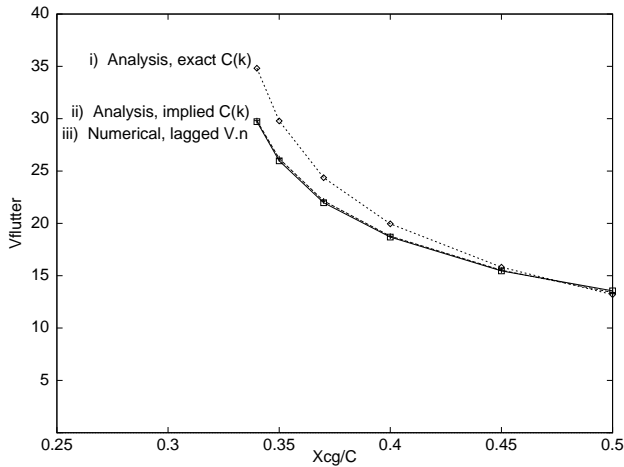
Fig. 12   Flutter speeds predicted analytically with $C_{\mathrm{exact}}(k)$ and $C_{\mathrm{implied}}(k)$, and by present method.

Violent Gust Encounter

This example is a time-marched calculation of a lightweight sailplane flying at 70 ft/s through a small but intense "thermal", with 30 ft/s peak vertical velocity. Figure 13 shows the sailplane location before and after the encounter. Figure 14 is a snapshot from an on-screen movie showing the deformed geometry. The ability to rapidly generate and display such simulations allows extensive investigation of possible structural or control failure modes.
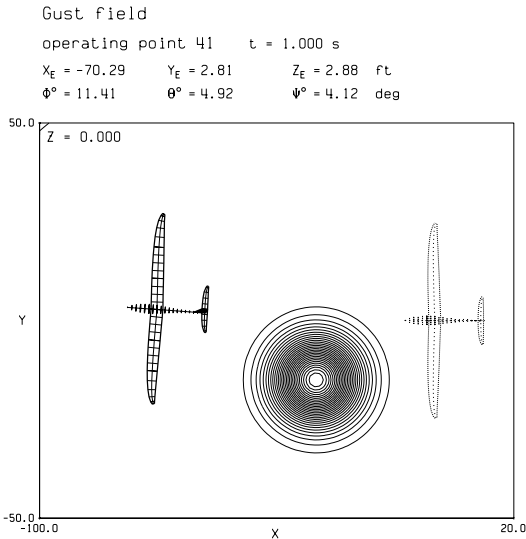

Fig. 13   Sailplane flying though small intense gust "thermal", indicated by vertical-velocity contours.

Figure 15 shows the peak extensional strain, mostly associated with M_c, with the spanwise distributions for all time snapshots overlaid. The envelope of all the curves immediately indicates the likely failure area.
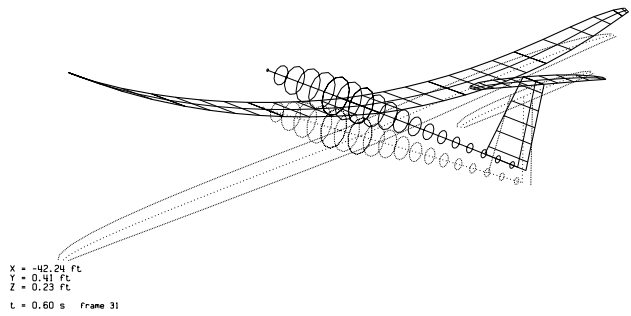
Fig. 14   Deformed sailplane midway during vertical gust encounter.

Interestingly, the maximum strain occurs near the wingtip *opposite* the vertical gust, due to a whip-like elastic response of the wing. This rather counterintuitive result shows the importance of dynamic loading analysis in structural sizing of flexible aircraft.
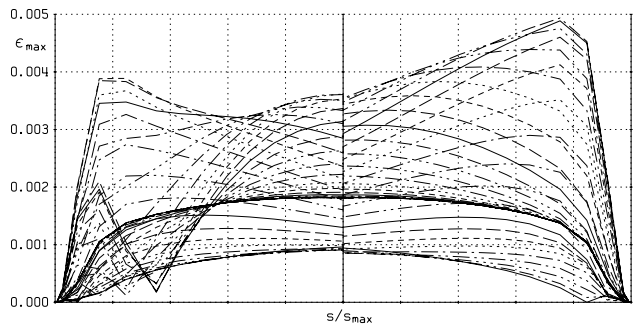
Fig. 15   Strain distributions for 40 time snapshots during gust encounter.

Since the structural properties are all one-dimensional functions along the beam, it is feasible to interactively modify the wing's geometry or structure (e.g. $\bar{c}$, EI_{cc}), on the screen. One example might be to alleviate the weak spot indicated in Figure 15. The gust-encounter simulation can then be immediately recomputed to test or confirm the redesign.

Root-Locus Analysis

An eigenmode analysis of the sailplane for each of 14 flight velocities produces the root-locus map shown in Figure 16. Since flight dynamics modes as well as structural modes are described by the overall system Jacobian, both types of modes appear, although in this case the distinctions are not clear. The short-period and 1st-bending modes are quite similar in appearance, and relatively close in frequency. This mingling is not uncommon in highly-flexible aircraft, and can considerably complicate autopilot design.

The present method does not distinguish between

12

the classical flight dynamics modes and structural modes. In fact, the term "structural mode" is really a misnomer, since the aerodynamic circulation variables A_k always participate. Coupling of in-vacuo modes is not an issue — all eigenmodes are guaranteed to be decoupled. This feature allows rapid testing of candidate control laws with a good degree of confidence, since the full state vector is always involved and *all* dynamical modes of the system are represented.

As in the gust encounter case, quick design changes can be made and re-analyzed. Here, a typical redesign might aim to modify the aircraft's natural vibration modes (via EI_{cc}, GJ, μ, ι_{nn}, etc.), or to modify the distribution and magnitude of the forcing loads (via $dc_\ell/d\delta_F$). This allows rapid tailoring of the aircraft's dynamic response in concert with the control-law design, to give a better behaved closed-loop system.

References

[1] Rodden, W., "MCS/NASTRAN Handbook for Aeroelastic Analysis I & II," Report MSR-57, The MacNeal-Schwendler Corporation, Los Angeles, CA, 1987.

[2] Johnson, W., "Development of a Comprehensive Analysis for Rotorcraft-I. Rotor Model and Wake Analysis." *Vertica*, Vol. 5, 1981, pp. 99–129.

[3] Minguet, P., *Static and dynamic behavior of composite helicopter rotor blades under large deflections*, Ph.D. thesis, MIT, June 1989.

[4] Drela, M., "Method for Simultaneous Wing Aerodynamic and Structural Load Prediction," *Journal of Aircraft*, Vol. 27, No. 8, Aug 1990.

[5] Theodorsen, T., "General Theory of Aerodynamic Instability and the Mechanism of Flutter," TR 490, NACA, 1935.

[6] Lehoucq, R., Sorensen, D., and Yang, C., *ARPACK User's Guide: Solution of Large Scale Eigenvalue Problems with Implicitly Restarted Arnoldi Methods*, SIAM Publications, Philadelphia, 1998, ISBN 0-89871-407-9.
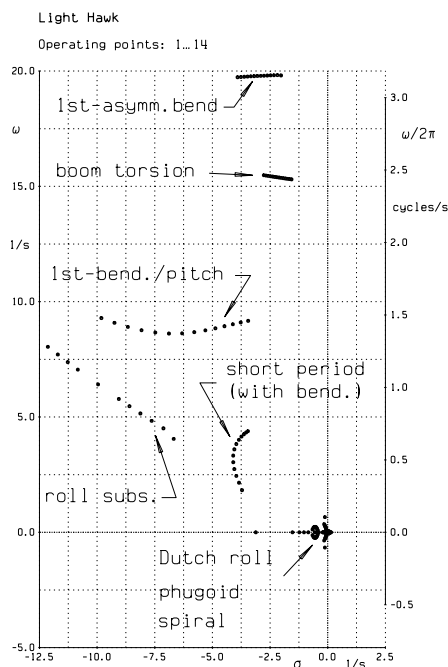
Fig. 16   Root locus map for range of velocities.

Conclusions

This paper presented an aircraft simulation model with aerodynamics, structures, flight dynamics, and control laws fully and nonlinearly coupled. Simplifications were employed where appropriate to reduce the computational size of the model to allow interactive execution. The coded implementation provides an effective platform for rapid and effective preliminary design.

13